Electronic Supplementary Information

Designing a mechanically driven spin-crossover molecular switch via organic embedding

S. Bhandary,[1,*] J. M. Tomczak,[2] A. Valli[3]

[1] School of Physics, Trinity College Dublin, The University of Dublin, Dublin 2, Ireland
[2] Institute of Solid State Physics, Vienna University of Technology, 1040 Vienna, Austria
[3] Institute for Theoretical Physics, Vienna University of Technology, 1040 Vienna, Austria

* E-mail: sumanta.bhandary@tcd.ie

ELECTRONIC STRUCTURE SIMULATIONS

The workflow of our ab-initio and many-body simulations is depicted in Fig. S1. In the following we discuss in detail the individual steps.

DFT computational details

We have used Vienna ab-initio Simulation Package[1] (VASP) for the DFT calculations. The device is periodic in the x-direction. In the y-direction the separation from the periodic image is more than 16Å. The vacuum in the z-direction is 20Å. Ionic positions of all the structures have been optimized. The plane-wave projector augmented wave basis was used in the Perdew-Burke-Ernzerhof generalized gradient approximation (PBE-GGA) for the exchange correlation potential. The plane-wave cutoff energy used was 400 eV. A $10{\times}1{\times}1$ Monkhorst Pack k-mesh was used for the integration in the Brillouin zone. Atoms were relaxed until the Hellmann-Feynman forces were below 0.01 eV/Å. As electronic correlations play a crucial role in determining the SCO, it is reasonable to include their feedback also in the structural relaxation. We have performed structural relaxation within the DFT+U formalism[2] with interaction parameters $U = 4.0$ eV and $J = 1.0$ eV, which take into account the static contributions of the Coulomb repulsion, and, to some extent, can already describe the SCO. It has to be noted that the parameters for the many-body calculations, i.e., the hybridization functions and crystal fields (see also below), are obtained from non-spin polarised (i.e., *sans* U) calculations using those relaxed structures (obtained in DFT+U) while dynamical correlation effects are
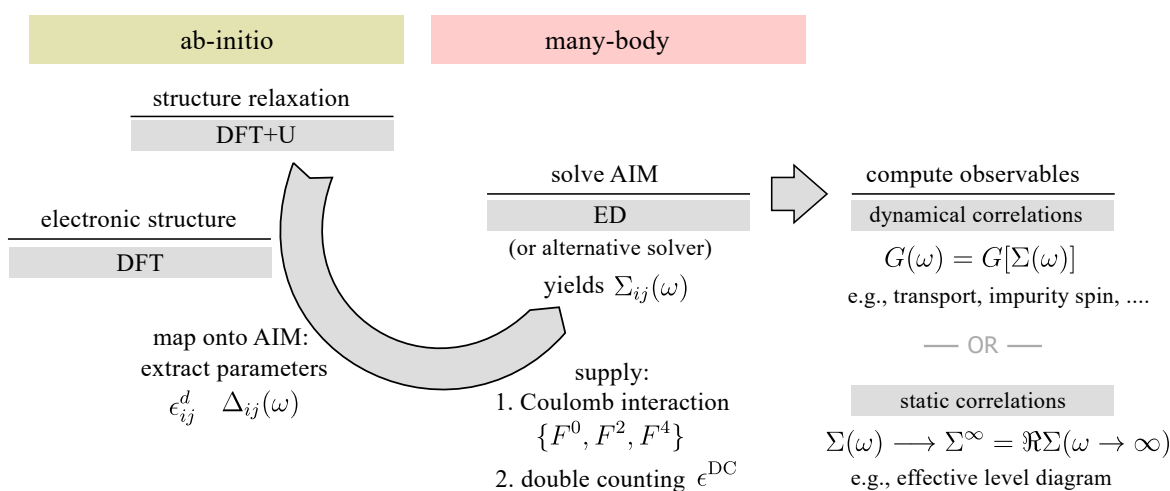

FIG. S1. Flowchart of the ab-initio and many-body calculations. For each step, we indicate the level of theory employed. The structural relaxation is performed within DFT+U, to take into account the effect of the Coulomb repulsion. The electronic structure calculation needed to extract the parameters of the impurity model is performed at the level of DFT (i.e., *sans* U) since electronic correlations within the Fe-3d multiplet are recovered at a higher level of theory within the many-body calculations.

incorporated within the explicit many-body techniques.

Many-body effects: DFT++

To investigate the molecular spin-crossover, we have employed a combination of DFT and many-body techniques within a multi-orbital Anderson impurity model (AIM), which is usually referred to as a DFT++ method.[3]

Anderson impurity model

A realistic description of the complete system is obtained within DFT. This allows to extract *ab-initio* parameters to describe a correlated sub-space, i.e., the impurity, corresponding to the Fe-$3d$ multiplet, which is coupled to a bath, corresponding to the rest of the system, including both the porphyrin ligands and the zGNR leads, via a retarded hybridization function. The impurity is supplemented with a Coulomb interaction, and the resulting many-body problem can be solved numerically. The Hamiltonian of the AIM can be expressed as

$$H = \sum_{ij} \epsilon_{ij}^d d_{i\sigma}^\dagger d_{j\sigma} + \frac{1}{2} \sum_{ijkl} \sum_{\sigma\sigma'} U_{ijkl} d_{i\sigma}^\dagger d_{j\sigma'}^\dagger d_{l\sigma'} d_{k\sigma}$$
$$+ \sum_{im} \sum_\sigma (V_{im} c_{m\sigma}^\dagger d_{i\sigma} + h.c.) + \sum_m \sum_\sigma \epsilon_m c_{m\sigma}^\dagger c_{m\sigma}, \tag{S1}$$

where $d_{i\sigma}$ ($d_{i\sigma}^\dagger$) denote the annihilation (creation) operators of an electron in impurity (Fe-$3d$) orbital i with spin σ, and $c_{m\sigma}$ ($c_{m\sigma}^\dagger$) denote the annihilation (creation) operators of an electron in bath orbital m with spin σ and energy ϵ_m. The coupling between Fe-$3d$ and bath orbitals is given by V_{im}. The matrix ϵ_{ij}^d describes the crystal field and U_{ijkl} represents the full Coulomb tensor within the Fe-$3d$ multiplet. The rotationally-invariant Coulomb interaction is parametrized via the Slater radial integrals[4,5] F^0, F^2, and F^4, such that $U = F^0$ and $J = \frac{1}{14}(F^2 + F^4)$, with the ratio $F^4/F^2 = 0.625$, yielding a spherically symmetric tensor.[6,7] In the presence of a crystal field, the spherical symmetry is lifted. This effect could be taken into account, e.g., within the constrained random phase approximation,[8] but we do not expect it to change any of the conclusions of our analysis.

Embedding the Fe-atom: Hybridization function

In order to calculate the hybridization function *ab-initio*, the Kohn-Sham Green's function G_{KS} is calculated from the Lehmann representation

$$G_{KS}(\omega) = \sum_{nk} \frac{|\psi_{nk}\rangle \langle \psi_{nk}|}{\omega + i\delta - \epsilon_{nk}}, \tag{S2}$$

where ψ_{nk} and ϵ_{nk} are the Kohn-Sham eigenstates and eigenvalues for band n and reciprocal-space point k, while δ is an infinitesimal broadening, indicating G_{KS} to be the retarded propagator. This Green's function is then projected onto a local (impurity) propagator G_0, evaluated on atom-centered, localized orbitals χ_i. In this basis, the local Green's function reads

$$G_0^{ij}(\omega) = \sum_{nk} \frac{\tilde{P}_{nk}^i (\tilde{P}_{nk}^j)^*}{\omega + i\delta - \epsilon_{nk}} \tag{S3}$$

where $P_{nk}^i = \langle \chi_i | \psi_{nk} \rangle$ are projection matrices normalized as

$$\tilde{P}_{nk}^i = \sum_j [O(k)]^{-1/2} P_{nk}^j, \tag{S4}$$

with the overlap operator

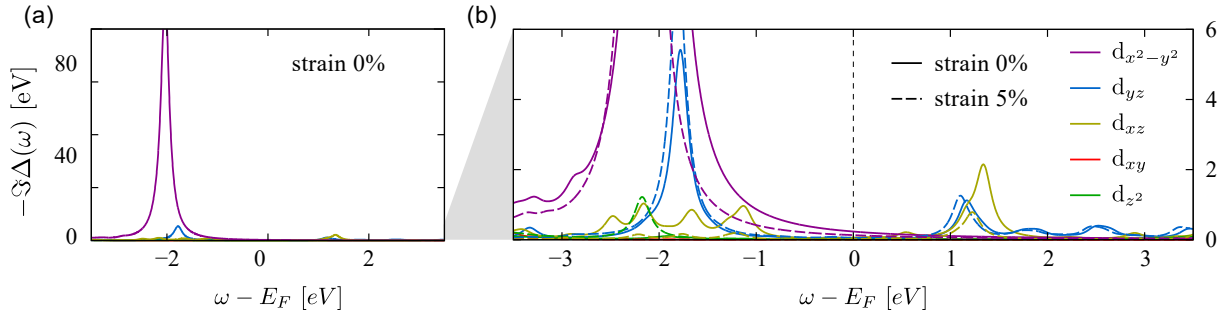$$O_{ij}(k) = \sum_n P_{nk}^i (P_{nk}^j)^*. \tag{S5}$$

FIG. S2. (a) Orbital-resolved hybridization function $\Delta(\omega)$ for the unstrained device. The $d_{x^2-y^2}$ peak at $\epsilon^b = -2.03$ eV dominates the frequency structure. (b) Evolution of the hybridization function across the SCO, at 0% (solid) and 5% (dashed lines) strain.
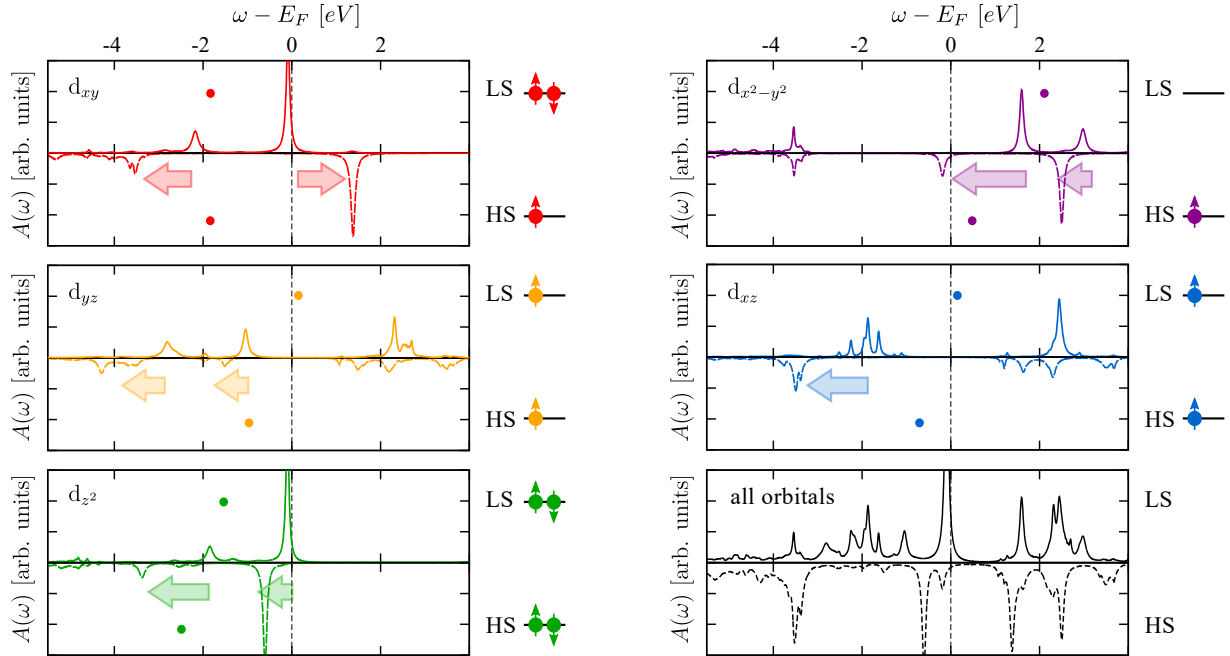

FIG. S3. Orbital-resolved and total many-body spectral functions for the LS (2% strain, respective top panels) and HS state (2.5% strain, bottom panels). Arrows indicate the shifting of individual spectral features between LS and HS while the dots indicate the energies of the corresponding single-particle state in the effective level diagram of Fig. S5. The dots qualitatively follow the centre of gravity of the different orbital characters, thus encoding the overall orbital shifts. On the right of each panel, we indicate the nominal spin configuration of the selected orbital and spin state. Note that the d_{xy} and d_{z^2} orbitals weakly hybridize with the ligands, therefore even though they display sharp resonances close to the Fermi level, their corresponding contributions in the transmission function are strongly suppressed, see Fig. S7.

Finally, the hybridization function is calculated from the local impurity Green's function from the expression

$$\Delta_{ij}(\omega) = \left[\omega + i\delta\right]\delta_{ij} - \epsilon_{ij}^d - \left[G_0^{-1}\right]_{ij}(\omega). \tag{S6}$$

Note that the hybridization function includes also off-diagonal terms if the projected Fe-3d orbital are not orthogonal (i.e., $\epsilon_{i\neq j}^d \neq 0$). In the current cases $\Delta_{i\neq j} \ll \Delta_{ii}$ for any pair (i, j), and neglecting these contributions yields an expression equivalent to the one given in the manuscript, yet projected on the localized Fe-3d orbitals. The diagonal elements of the hybridization function $\Delta_{ii}(\omega)$ are shown in Fig. S2, clearly indicating that the $d_{x^2-y^2}$ is the dominant contribution among them.

Spectral functions

In Fig. S3 we show the ED spectral functions for one strain below the spin-crossover (2% strain, LS) and one above (2.5% strain, HS), resolved into the individual Fe-3d orbitals. As indicated by the horizontal arrows, spectral features jump to significantly different positions when the spin-crossover is triggered. In particular, spectral weight of $d_{x^2-y^2}$ (d_{z^2}) character moves to (away from) the Fermi level, in congruence with our analysis of the transmission function in the main manuscript.

Numerical solution: ED vs. QMC

The AIM in Eq. (S1) can be solved with several numerical techniques, each with their advantages and disadvantages. Here we adopt exact diagonalization (ED) for the results presented in the manuscript and continuous-time Quantum Monte Carlo[9] (QMC) as a benchmark. A schematic representation of the ED and QMC algorithms is shown in Figs. S4(a,b) while results for the corresponding transmission function, are shown in Fig. S4(c). This comparison highlights a remarkable agreement for both 0% and 5% tensile strain, which correspond to LS and HS state configurations, respectively. This analysis shows that the physical scenario underlying the SCO in the zGNR-FeP-zGNR device is robust with respect to the details of our numerical calculations.

ED solver. As the ED solver is based on the Hamiltonian formalism, the dynamical hybridization function is discretized, i.e., approximated by a finite number of bath sites. The hybridization function in Fig. S2 is dominated by the diagonal $d_{x^2-y^2}$ contribution, and the second strongest hybridization is the d_{yz} one. Hence, for the ED calculations, it is sufficient to fit those two contributions with one pole each. This procedure yields the bath orbital energies ϵ^b and the corresponding coupling V for the $d_{x^2-y^2}$ and d_{yz} orbitals listed in Tab. I.

TABLE I. Anderson parameters of the ED calculations, for different values of uniaxial strain.

Parameters [eV]	Strain [%]						
	0	1	2	2.5	3	4	5
$V_{d_{x^2-y^2}}$	3.04	2.97	2.80	2.61	2.56	2.45	2.35
$\epsilon^b_{d_{x^2-y^2}}$	-2.03	-2.08	-2.13	-2.13	-2.14	-2.15	-2.18
$V_{d_{yz}}$	0.74	0.76	0.79	0.76	0.79	0.83	0.89
$\epsilon^b_{d_{yz}}$	-1.78	-1.80	-1.81	-1.80	-1.79	-1.79	-1.81

In the solution of the many-body problem, we include a double counting correction to compensate for the DFT contribution of the Coulomb interaction. We adopt the fully localised limit (FLL) form[10,11] given by

$$\epsilon^{\mathrm{DC}} = U\left(n - \frac{1}{2}\right) - \frac{J}{2}\left(n - 1\right) \tag{S7}$$

with n being the total impurity occupation. However, instead of considering the DFT-occupations, we obtain ϵ^{DC} in a charge self-consistent manner, i.e., we start with an initial guess of ϵ^{DC}, obtain new occupations in ED and calculate a new ϵ^{DC}. The process is iterated until we obtain a convergence over the total occupation.

The solution of the AIM yields a retarded self-energy matrix $\Sigma_{ij}(\omega)$ that takes into account the many-body effects within the Fe-3d multiplet. The corresponding many-body Green's function is given by

$$G^{-1}_{ij}(\omega) = \left[\omega + \imath\delta + \epsilon^{\mathrm{DC}}\right]\delta_{ij} - \epsilon^d_{ij} - \Delta_{ij}(\omega) - \Sigma_{ij}(\omega), \tag{S8}$$

which in turn allows to evaluate the transmission function and investigate the transport properties of the device, see below.

Note that in the DFT++ framework it is possible to obtain a paramagnetic solution, so that the Hamiltonian, the hybridization function, the self-energy, and eventually also the many-body Green's function, are not spin-polarized. In contrast to, e.g., DFT+U, this scheme allows us to describe a fluctuating local moment on the Fe atom and the transport properties across the SCO in the absence of any static magnetic order.

QMC solver. Within the QMC algorithm, the dynamical nature of the hybridization function can be fully taken into account, and the double counting correction is implemented by fixing the occupation of the Fe-3d manifold
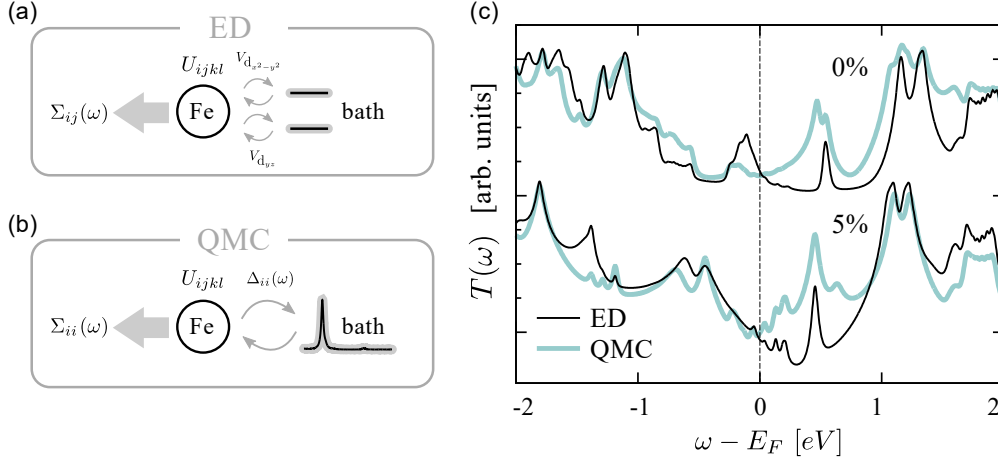
FIG. S4. Schematic representation of (a) ED and (b) QMC impurity solvers. (c) Transmission function at 0% and 5% tensile strain, obtained from many-body calculations with both solvers. The curves are shifted vertically for a better visibility.

$n = \sum_{i\sigma} \langle n_{i\sigma} \rangle$ to the values $n^{\mathrm{LS}} = 6.7$ and $n^{\mathrm{HS}} = 6.4$ electrons. These values are chosen in correspondence with the impurity occupations in ED for the two different spin-states. Due to technical complications, it is convenient to neglect the off-diagonal elements of the Hamiltonian and the hybridization function. As a result, the QMC self-energy becomes diagonal in orbital space, i.e., $\Sigma_{ij}(\omega) = \delta_{ij}\Sigma_{ii}(\omega)$. The remarkable agreement found between the QMC and ED data allows us to verify *a posteriori* that (i) the off-diagonal components of the self-energy have a negligible effect on the result, and (ii) the hybridization function is well approximated with two ED bath sites. In the context of a free FeP molecule, the convergence of spin-transition energy with the number of bath sites was checked in a previous publication,[12] further justifying our choice here. Let us also note that, in the case of QMC, an additional step is required, namely to analytically continue the Matsubara self-energy to the real-frequency axis via a maximum entropy method.[13]

Competition between ligand crystal field and Coulomb interaction

In order to have a better grasp of the competition between the ligand crystal field and the Coulomb interaction, one can extract an effective energy level diagram from the ED calculations. We consider an effective 7×7 Hamiltonian for the five Fe-3d and the two ligand orbitals, which in block-matrix form can be represented as

$$H_{\mathrm{eff}} = \begin{pmatrix} \epsilon^d & V \\ V^\dagger & \epsilon^b \end{pmatrix} + \begin{pmatrix} \Sigma^\infty & 0 \\ 0 & 0 \end{pmatrix}. \tag{S9}$$

In this notation, ϵ^d is a 5×5 matrix representing the crystal fields of the Fe-3d multiplet, ϵ^b is a 2×2 (diagonal) matrix with the ligand orbital energies, and V is a 2×5 matrix with only two non-zero elements, corresponding to the couplings $V_{\mathrm{d}_{x^2-y^2}}$ and $V_{\mathrm{d}_{yz}}$ defined above, while $\Sigma^\infty = \Re\Sigma(\omega \to \infty)$ is the static contribution to the many-body self-energy in the Fe-3d subspace. Since the parameters of the model depend on strain, we can define a family of Hamiltonians. For a given strain, the diagonalization of the respective Hamiltonian yields the eigenvalues $\{\epsilon_i\}$ corresponding to molecular orbitals (MOs) with Fe-3d and ligand mixed character.

In Fig. S5(a) we show the MO eigenvalues obtained by considering the effect of the ligands *without* the self-energy contribution. Starting from the isolated subspaces of the unstrained device, due to the couplings between the d$_{x^2-y^2}$ and d$_{yz}$ orbitals and their bath sites, the system creates bonding and anti-bonding MOs. However, tensile strain has surprisingly very little effect on the energy level diagram. Even at 5% strain, the anti-bonding MO with predominant d$_{x^2-y^2}$ character is still far above the Fermi level, $\epsilon_{\mathrm{d}_{x^2-y^2}} \approx 1.8$ eV. This suggests that the structural changes alone are not able to trigger the SCO. Including the self-energy contributions the scenario changes substantially, as shown in In Fig. S5(b). The ligand field splitting $\Delta_{\mathrm{LF}} = \epsilon_{\mathrm{d}_{x^2-y^2}} - \epsilon_{\mathrm{d}_{xy}}$ is reduced upon strain and at the same time $\epsilon_{\mathrm{d}_{x^2-y^2}} \approx E_F$, thus triggering the SCO.

It is interesting to compare the ligand fields to the Coulomb energy difference $\Delta_{\mathrm{Coulomb}}$ between the atomic LS and HS states. Although we consider the full Coulomb tensor U_{ijkl} in the numerical calculations, an intuitive picture can
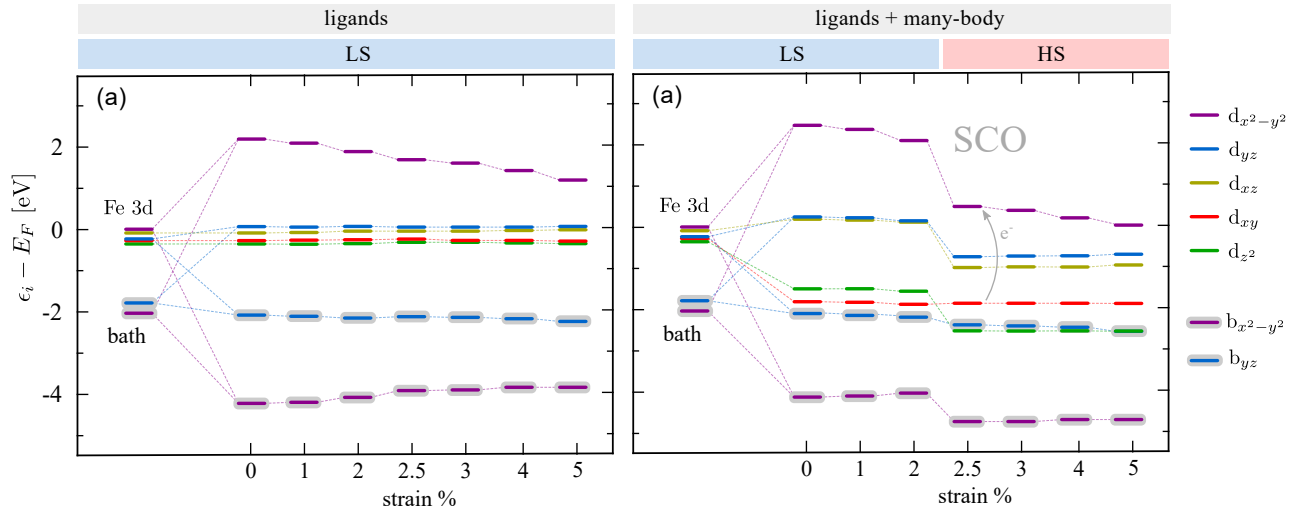
FIG. S5. Effective level diagram for the Fe-$3d$ multiplet with two bath site model within the static approximation for the self-energy. Effect of the ligand field (a) alone and (b) together with many-body effects. The latter is necessary to trigger the SCO at realistic values of tensile strain. Both (a) and (b) use, for a given strain, the same structure.
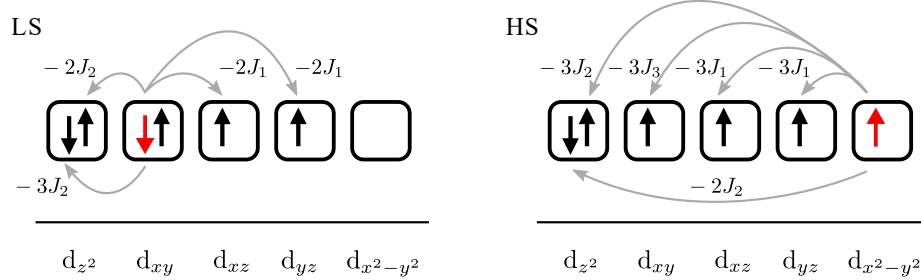

FIG. S6. Within the density-density approximation, the Coulomb energy difference between the atomic LS and HS states is given by $\Delta_{\text{Coulomb}} = 2J_1 + 3J_3$. Since U is the same for all orbitals, the energy difference is obtained from the variation of exchange interactions (grey arrows) associated to the electron promoted from the d_{xy} to the $d_{x^2-y^2}$ orbital across the SCO (marked in red).

already be obtained within a (simplified) density-density approximation, under the assumption of a cubic ligand field. Then, the Coulomb interaction reduces to

$$U_{iiii;\sigma\sigma} = U_0$$
$$U^{i \neq j}_{ijji;\sigma\sigma'} = U_0 - 2J_{ij} - J_{ij}\delta_{\sigma\sigma'}, \tag{S10}$$

and is given in terms of an intra-orbital interaction U_0 (which is the same for all orbitals) and four exchanges $J_{ij} = \{J_1, J_2, J_3, J_4\}$. Including the term of the Coulomb tensor beyond the density-density approximation cannot be done at this intuitive level, because they conserve neither the spin-orbital charge $n_{i\sigma}$ nor the spin projection S^z_i quantum numbers. An extensive discussion of the Coulomb parametrization can be found in the literature.[4–7]

Under the above conditions, the Coulomb energy difference between the atomic LS and HS states in terms of the exchange parameters is given by

$$\Delta_{\text{Coulomb}} = E^{\text{LS}}_{\text{Coulomb}} - E^{\text{HS}}_{\text{Coulomb}} = 2J_1 + 3J_3. \tag{S11}$$

The physical interpretation of this result is shown in Fig. S6 and is summarized as follows. The LS and HS states differ in the occupation of the d_{xy} and $d_{x^2-y^2}$ orbitals. Since the direct Coulomb interaction is the same for each pair of orbitals, its contribution is the same in both states. However, with respect to the LS state, in the HS state there is an additional interaction term $-3J_1$ between the parallel d_{xy} and $d_{x^2-y^2}$ spins and two additional terms $-J_1$ since the spin in $d_{x^2-y^2}$ is now parallel to those in the d_{xz} and d_{yz} orbitals. We find that $\Delta_{\text{Coulomb}} \sim 2.83$ eV, which is

of the same order of magnitude as the ligand field splitting between the d_{xy} and $d_{x^2-y^2}$ orbitals. Hence, even this approximate picture confirms the competition between the ligand field and the Coulomb interaction to be at the root of the SCO phenomenology. Moreover, this procedure intuitively shows that the many-body renormalization of the ligand field plays a crucial role in the determining which spin state becomes energetically favorable, and at which critical strain value.

TRANSPORT SIMULATIONS

Effective Fe model for transport calculations

In the standard quantum transport formalism, the transmission function is evaluated through the Landauer formula[14,15]

$$T(\omega) = T(\omega) = \text{Tr}\big[\Gamma^L(\omega)G^\dagger(\omega)\Gamma^R(\omega)G(\omega)\big], \tag{S12}$$

where $G^{(\dagger)}(\omega)$ denotes the retarded (advanced) real-space Green's function, which is a matrix in the basis spanning the whole scattering region, and $\Gamma^\alpha(\omega) = \imath[\Sigma^\alpha(\omega) - \Sigma^{\dagger\alpha}(\omega)]$ represents the coupling to the leads, given in terms of the embedding self-energy $\Sigma^\alpha(\omega)$.

In general, this approach requires a projection of the whole scattering region from plane-waves onto Wannier orbitals, which is far from trivial.[16,17] In particular, for complex devices such as the one considered here, it becomes a prohibitive task. Hence, we follow an alternative route, taking advantage of the local projection onto the Fe impurity, which was used to evaluate the many-body self-energy. We stress, that the many-body self-energy is dynamical and non-hermitian and required us to implement the Landauer formula for general, interacting Green's functions.

We evaluate the Landauer formula of Eq. (S12) through the Fe-3d orbitals, for which the Green's function includes the many-body effects stemming from the Coulomb interaction[8,14,15,18,19] and treat the rest of the device as the leads. Physically, this corresponds to considering the transmission channels in which the electrons tunnel coherently through the correlated Fe atom, and the transmission function will qualitatively mirror the spectral properties of the impurity.[14,15] In practice, we define the embedding self-energies as $\Sigma^L(\omega) + \Sigma^R(\omega) = \Delta(\omega)$ and, since the device is symmetrical along the transport direction, the most natural choice is to assume $\Sigma^L = \Sigma^R$. In this framework, the transmission function (per spin) becomes

$$T(\omega) = \sum_{\ell\ell'rr'} \Gamma^L_{\ell\ell'}(\omega)G^a_{\ell'r}(\omega)\Gamma^R_{rr'}(\omega)G^r_{r'\ell}(\omega) \tag{S13}$$

where indices runs over all orbitals of the Fe-3d multiplet. Each orbital contribution to the transmission function is obtained by setting to zero all other components of the coupling matrices Γ^L and Γ^R, thus isolating the corresponding element of the Green's function. Hence, for each component α the transmission is given by

$$T_\alpha(\omega) = \Gamma^L_{\alpha\alpha}(\omega)G^a_{\alpha\alpha}(\omega)\Gamma^R_{\alpha\alpha}(\omega)G^r_{\alpha\alpha}(\omega). \tag{S14}$$

Note that since neither the embedding self-energy nor the Green's function itself are modified in this procedure, the sum over (diagonal and off-diagonal) channels yields the full transmission function.

Upon application of a bias voltage V_b, the electric current (per spin) driven through the Fe atom is given by

$$I = \frac{e}{h} \int_{-\infty}^{\infty} d\omega\, T(\omega)\big[f_L(\omega) - f_R(\omega)\big], \tag{S15}$$

where e is the electron charge, h is Plank's constant. The Fermi-Dirac distribution function for the L and R electrodes is given by

$$f_{L/R}(\omega) = \frac{1}{1 + \exp[(\omega - \mu_{L/R})/(k_BT)]}, \tag{S16}$$

where $\mu_L - \mu_R = eV_b$ is the symmetric bias drop, k_B is the Boltzmann constant and T the temperature. We assumed a temperature broadening $k_BT = 25$ meV, i.e., close to room temperature, but the results are qualitatively identical to those obtained for smaller broadenings. The current in Eq. (S15) is evaluated neglecting the dependence of the transmission function on the bias voltage, i.e., $T(E, V_b) \approx T(E)$, which is a reasonable assumption in the low-bias regime.[14,15,20]

  In principle, there are also other transmission channels through the device, which do not involve the Fe atoms. The electrons are instead transported through the organic framework of the porphyrin molecule. Those transmission channels display resonances far (at least ≈ 1 eV) from the Fermi level, corresponding to the molecular orbitals with dominant porphyrin C character. Since the ligands states are described by the hybridization function, Eq. (S6), they can be observed in the spectral function of Fig. S3. Within the considered bias window $[-eV_b/2, eV_b/2]$, with eV_b up to 0.5 eV, the off-resonant contributions of those channels constitute a background signal in the transmission function (and hence in the electric current). The effects of strain on such a background are certainly negligible with respect to the dramatic changes induced by the SCO due to the appearance of the Fe-$d_{x^2-y^2}$ resonance at the Fermi level.
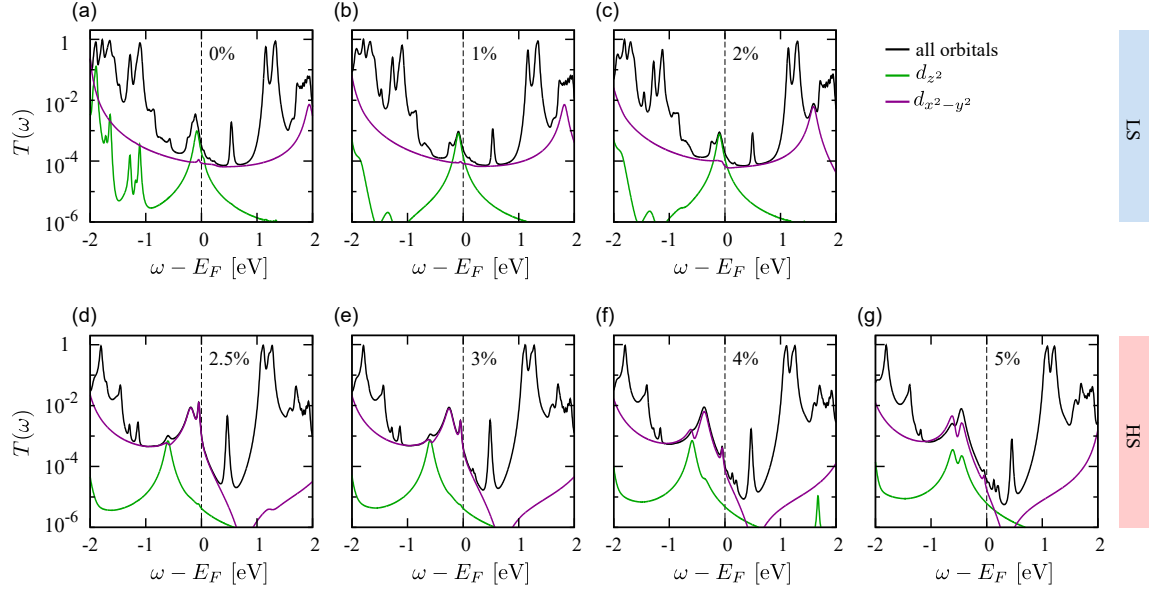

FIG. S7. Relevant d_{z^2} and $d_{x^2-y^2}$ contributions to the transmission functions for all strains.
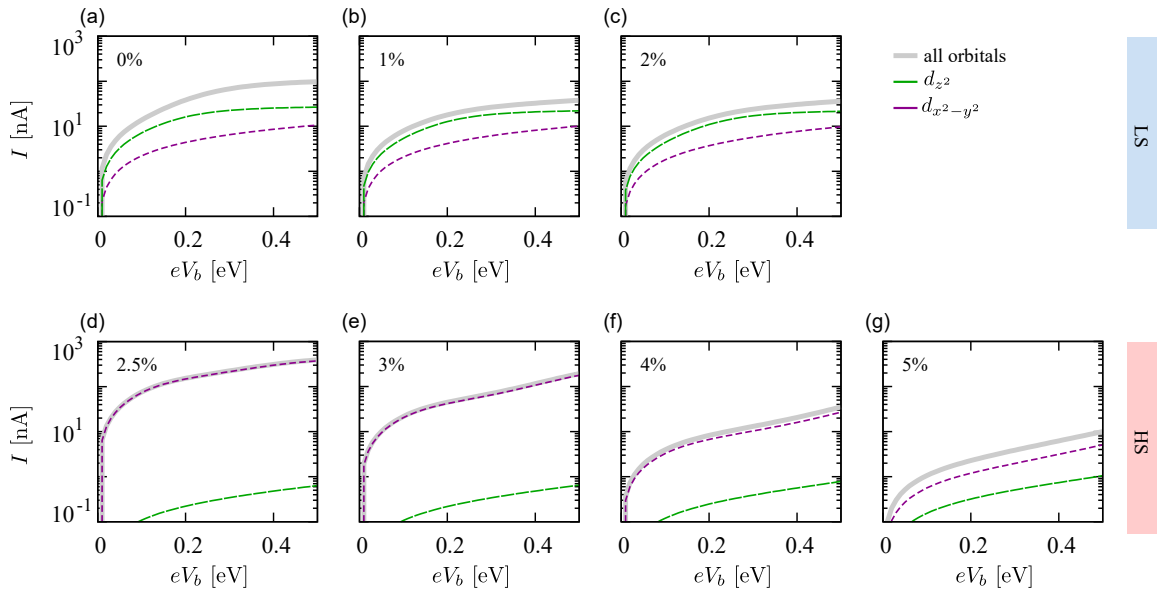

FIG. S8. Relevant d_{z^2} and $d_{x^2-y^2}$ contributions to the electric current for all strains as a function of the external bias.

Strain evolution of pertinent orbital contributions to the transport properties

The changes in the electronic structure of the Fe atom across the SCO directly affect the transport properties of the device. This is evident when considering the orbital resolved contributions to the transmission function, as shown in Fig. S7 for all values of strain. In the LS state, Fig. S7(a-c) the resonance corresponding to the unoccupied antibonding $d_{x^2-y^2}$ orbital lies ≈ 2 eV above the Fermi level. Upon applied strain, the resonance progressively shifts towards the Fermi level. At the SCO, the $d_{x^2-y^2}$ resonance jumps and is pinned to the Fermi level, Fig. S7(d), and dominates the transmission function in the HS state. Further increasing the strain suppress the $d_{x^2-y^2}$ resonance, as spectral weight is shifted below the Fermi level, thus reducing the transmission.

The corresponding trend is also observed in the electric current, which is shown in Fig. S8(a-g) for all values of strain. Across the SCO, the discontinuous behavior of the I-V characteristics is associated with the change in the character of the dominant contribution, from mainly d_{z^2} in the LS state to $d_{x^2-y^2}$ in the HS state. Since the current is dominated by a resonant contribution close to the Fermi level for all values of strain, the behavior of the I-V characteristics follows closely the one of the transmission at the Fermi level, shown in Fig. 4(e) of the manuscript.

---

[1] G. Kresse and J. Furthmüller, Phys. Rev. B **54**, 11169 (1996).
[2] A. I. Liechtenstein, V. I. Anisimov, and J. Zaanen, Phys. Rev. B **52**, R5467 (1995).
[3] M. Karolak, T. O. Wehling, F. Lechermann, and A. I. Lichtenstein, Journal of Physics: Condensed Matter **23**, 085601 (2011).
[4] J. C. Slater, Physical Review **34**, 1293 (1929).
[5] J. C. Slater, *Quantum Theory of Atomic Structure* (McGraw-Hill, New York, 1960).
[6] M. Karolak, Ph.D. thesis, Universität Hamburg, (Hamburg) (2013).
[7] A. Valli, M. P. Bahlke, A. Kowalski, M. Karolak, C. Herrmann, and G. Sangiovanni, Phys. Rev. Research **2**, 033432 (2020).
[8] D. Jacob, Journal of Physics: Condensed Matter **27**, 245606 (2015).
[9] E. Gull, A. J. Millis, A. I. Lichtenstein, A. N. Rubtsov, M. Troyer, and P. Werner, Rev. Mod. Phys. **83**, 349 (2011).
[10] A. I. Liechtenstein, V. I. Anisimov, and J. Zaanen, Phys. Rev. B **52**, R5467 (1995).
[11] M. T. Czyżyk and G. A. Sawatzky, Phys. Rev. B **49**, 14211 (1994).
[12] S. Bhandary, M. Schüler, P. Thunström, I. di Marco, B. Brena, O. Eriksson, T. Wehling, and B. Sanyal, Phys. Rev. B **93**, 155158 (2016).
[13] M. Jarrell and J. Gubernatis, Physics Reports **269**, 133 (1996).
[14] Y. Meir and N. S. Wingreen, Phys. Rev. Lett. **68**, 2512 (1992).
[15] A. Droghetti and I. Rungger, Phys. Rev. B **95**, 085131 (2017).
[16] K. S. Thygesen and K. W. Jacobsen, Chemical Physics **319**, 111 (2005).
[17] M. Strange, I. S. Kristensen, K. S. Thygesen, and K. W. Jacobsen, The Journal of Chemical Physics **128**, 114714 (2008).
[18] A. Valli, A. Amaricci, V. Brosco, and M. Capone, Nano Lett. **18**, 2158 (2018).
[19] A. Valli, A. Amaricci, V. Brosco, and M. Capone, Phys. Rev. B **100**, 075118 (2019).
[20] H. Ness, L. K. Dash, and R. W. Godby, Phys. Rev. B **82**, 085426 (2010).